International Journal of Heat and Mass Transfer 192 (2022) 122908

Contents lists available at ScienceDirect

International Journal of Heat and Mass Transfer

journal homepage: www.elsevier.com/locate/hmt

Abnormal in-plane thermal conductivity anisotropy in bilayer α-phase tellurene

Yanhua Cheng[a,b], Xiaolong Yang[c], Zherui Han[b], Wenzhuo Wu[d], Xiaobing Luo[a,*], Xiulin Ruan[b,*]

[a] School of Energy and Power Engineering, Huazhong University of Science and Technology, Wuhan 430074, PR China
[b] School of Mechanical Engineering and the Birck Nanotechnology Center, Purdue University, West Lafayette, Indiana 47907-2088, USA
[c] Chongqing Key Laboratory of Soft Condensed Matter Physics and Smart Materials, College of Physics, Chongqing UNIVERSITY, Chongqing 401331, PR China
[d] School of Industrial Engineering, Purdue University, West Lafayette, IN 47907-2023, USA

ARTICLE INFO

Article history:
Received 20 December 2021
Revised 9 March 2022
Accepted 5 April 2022

ABSTRACT

In layered materials, it is well known that the cross-plane or cross-chain (CC) thermal conductivity is lower than that of the in-plane or along-chain direction due to weaker bonding in the cross-plane or CC directions. In this work, surprisingly, we predict using first-principles that the CC thermal conductivity $\kappa_\perp$ is higher than the along-chain thermal conductivity $\kappa_\parallel$ with a $\kappa_\perp/\kappa_\parallel$ ratio of 1.174 in bilayer α-phase tellurene (2L-αTe), an emerging 2D material that has recently drawn extensive interest due to its intriguing electronic, thermoelectronic, and piezoelectronic properties. Also, the room-temperature $\kappa_\perp$ and $\kappa_\parallel$ of 2L-αTe are 5.69 W/mK and 4.85 W/mK, which are 251% and 31% enhanced from that of bulk Te, respectively. A detailed analysis of lattice structure, phonon spectra, and electron properties of 2L-αTe and bulk Te is provided. We find that the larger lattice shrink in CC direction and the change in band angle lead to stiffened phonons and weaker anharmonicity, which in turn yield higher phonon group velocity and longer phonon lifetime in CC direction for 2L-αTe, resulting in the enhanced thermal conductivity and the anomolus thermal anisotropy. Crystal orbital Hamiltan population (COHP) and electron localization function (ELF) analysis demonstrate the enhancement of the strength of "covalent-like quasi-bonding" (CLQB) in CC direction of 2L-αTe, which is accompanied by the lattice shrink in CC direction and the change of band angle. Our study identifies a case of unexpected anisotropic thermal transport in 2D materials, and sheds light on the improvement of thermal conductivity isotropy in 2D materials for the thermal management of electronic devices.

1. Introduction

Tellurene, or two-dimensional (2D) tellurium, is a new member of the 2D material family [1,2] and has attracted extensive interest due to its intriguing properties, such as strain-induced modulated bandgap [3–8], outstanding piezoelectricity [9,10], stable photoresponse performance [11–14], excellent thermoelectric performance [8,15-19], and potential for field-effect transistors [20]. With the device size decreasing to nanoscale, thermal management plays an increasingly important role in these applications. As a result, thermal transport properties are highly relevant to the industrial application of tellurene.

Tellurene is a phase transition material and found to have at least five stable or metastable phases, among which α-, β-, and γ-phases are relatively stable [2,6,9,10,21]. Specifically, for monolayer tellurene, β- and γ-phases are stable while α-phase is not; on the contrary, for two- and multi-layer tellurene, α-phase is most stable [11]. It is noteworthy that there are two different naming methods for the phases. One was originated from Zhu et al. [2] and the other from Wang et al. [10] and Xiang et al. [6]. Here we follow the second naming convention. Recently, the thermal and thermoelectric properties of monolayer β- and γ-phase tellurene have been comprehensively studied by simulations and experiments [8,15-18,22-25]. In a previous work co-authored by a subset of the current authors [25], tellurene examples with different thicknesses (as thin as ~30 layers) were fabricated and measured to exhibit prominent anisotropic thermal conductivity in along-chain (AC) and cross-chain (CC) directions, which is consistent with theoretical results. However, most of these works have been focused on the monolayer β- and γ-phase, leaving the thermal transport properties of 2D α-phase unexplored.

* Corresponding authors.
E-mail addresses: luoxb@hust.edu.cn (X. Luo), ruan@purdue.edu (X. Ruan).

https://doi.org/10.1016/j.ijheatmasstransfer.2022.122908
0017-9310/

In this work, we focus on the thinnest stable α-phase tellurene, i.e., bilayer α-phase tellurene (2L-αTe) [11]. Our first-principles calculations show that at room temperature in the two in-plane directions, CC and AC, thermal conductivities are 5.69 W / mK and 4.85 W / mK, respectively, enhanced by 251% and 31% compared to bulk Te and showing an abnormal anisotropy ratio $\kappa_\perp/\kappa_\parallel$ of 1.174. It should be noted that in bulk Te, the CC and AC thermal conductivities are 1.62 W/mK and 3.70 W/mK respectively with a $\kappa_\perp/\kappa_\parallel$ ratio of 0.439 [25]. In layered materials, it is well known that the cross-plane or CC thermal conductivity is lower than that of the in-plane or AC direction because of the weaker bonding in the cross-plane or CC directions. For example, the radial or cross-plane thermal conductivities of carbon nanotube bundles and graphite are two orders of magnitude lower than their axial or in-plane thermal conductivities [26,27], and the thermal conductivity ratios $\kappa_\perp/\kappa_\parallel$ of bulk selenium and tellurium are 0.287 [1] and 0.439 [25], respectively. In a recent report of less thermally anisotropic 2D material hybrid perovskite butylammonium lead iodide (BA_2PbI_4, BA = $C_4H_9NH_3^+$), $\kappa_\perp/\kappa_\parallel$ is 0.633 [28] which is still smaller than 1. In contrast, our bilayer α-phase tellurene results show an abnormal anisotropy ratio $\kappa_\perp/\kappa_\parallel$ above 1 with a value of 1.174. To explain the origin of the anomalous thermal conductivity anisotropy in 2L-αTe, lattice structures, phonon dispersion relations, phonon transport properties, and electronic properties are subsequently explored. According to our analysis, the higher phonon group velocity and longer phonon lifetime in CC direction lead to the anomalous thermal anisotropy of 2L-αTe, which originates from the reduction of interchain distance of the lattice and the change of the bond angle. The electronic origin of this anisotropy in κ is the strengthening of the "covalent-like quasi-bonding" (CLQB) in 2L-αTe [11,29], which is demonstrated by the crystal orbital Hamiltan population (COHP) and electron localization function (ELF). The formation of CLQB is attributed to wavefunction hybridization and lone electron pair interaction. Our predicted thermal conductivities and their unexpected anisotropy provide important insights to electronic, optoelectronic, and thermoelectric devices based on 2L-αTe, and could inspire experimental studies on this material system and further research in other 2D material systems.

2. Methods

In the framework of the Boltzmann transport equation (BTE) [30,31], the lattice thermal conductivity κ can be obtained by

$$\kappa=\frac{1}{k_B T^2}\frac{1}{8\pi^3}\sum_n\int_{BZ} f_0(\omega_{n,\mathrm{q}})[f_0(\omega_{n,\mathrm{q}})+1]\upsilon_{n,\mathrm{q}}^2\hbar^2\omega_{n,\mathrm{q}}^2\tau_{n,\mathrm{q}}d\mathrm{q}, \quad (1)$$

where $\upsilon_{n,\mathrm{q}}$, $\omega_{n,\mathrm{q}}$, and $\tau_{n,\mathrm{q}}$ are the phonon group velocity, frequency, and lifetime in the phonon branch n with the reciprocal vector q over the first Brillouin zone (BZ). f_0 denotes the occupation number of phonons following the Bose-Einstein distribution. To obtain accurate κ, we employ an iterative scheme starting from the relaxation time approximation (RTA). Within the RTA, the total phonon scattering rates τ^{-1} are obtained by summing up the three-phonon scattering rates $\tau_3^{-1}$and the isotopic scattering rates τ_{iso}^{-1} based on Matthiessen's rule. Four-phonon scattering is not included in this study because the computational cost of this case is far beyond our current computational capability.

Vienna Ab-initio Simulation Package (VASP) [32,33] with the projector augmented wave (PAW) formalism is used to carry out the interatomic force constant (IFC) calculations. The generalized gradient approximation (GGA) to the exchange-correlation potential in the Perdew-Burke-Ernzerhof (PBE) [34] form is applied. A plane wave cut-off energy of 500 eV is used for lattice structure optimization and IFCs calculations. The total energy and Hellmann-Feynman force convergence criteria are set to 10^{-8} eV and 10^{-4} eV/Å. The Tkatchenko and Scheffler (DFT-TS) method [35] is chosen to correct the van der Waals effect for 2L-αTe, which has been proven to show better agreement with the experimental data [10]. For the calculation of 2L-αTe, a 6 × 6 × 1 supercell is built, with a 7 × 5 × 1 Monkhorst-Pack k-mesh applied. Phonopy [36] and Thirdorder [37] are utilized to extract the 2nd and 3rd IFCs, considering up to the fifth nearest neighbor. We use Sheng-BTE [37] code with the iterative solution to solve the phonon BTE, with a q-mesh of 130 × 100 × 1. In order to eliminate the interactions between tellurene layers and its mirror induced by the periodic boundary conditions, a vacuum spacing of about 30 Å is introduced. For bulk Te, a 4 × 4 × 4 supercell is built to perform the IFCs calculations using a 5 × 5 × 5 Monkhorst-Pack k-mesh, and a 24 × 24 × 24 q-mesh is set to solve the BTE. The convergence of κ with different q-mesh has been tested, as shown in Fig. S1.

3. Results and discussion

3.1. Lattice structures and phonon dispersions

As shown in Fig. 1(a-c), the lattice of bulk Te is composed of stacked helical Te-chains parallel to [0001] direction. The in-chain atoms are connected by covalent bonds, while the adjacent chains are connected by a type of bonding that is not clearly identified yet. In the later sections, this kind of bonding is observed and discussed based on the thermal properties of 2L-αTe and bulk Te. Our results support the proposal of CLQB [11,29], which is an interaction stronger than van der Waals (vdW) force but slightly weaker than covalent bonds. Bulk Te belongs to the $P3_121$ space group, possessing a three-fold screw axis along [0001] direction. The alignment of Te-chains forms a hexagonal shape. The lattice constants and bond lengthes are illustrated in Fig. 1(a-c). Angle α is defined as the angle between the specific Te-Te bond and the CC direction (Fig. 1f), which can intuitively imply the interacting strength in CC direction. Obviously, the smaller α is, the stronger the interaction is in CC direction. For bulk, α is 51.087°

2L-αTe structure has similarity as well as significant distinctions from that of bulk Te, as shown in Fig. 1(d-f). Cutting bulk Te by $(10\bar{1}0)$ planes (Fig. 1a) and separating two neighbor layers of Te-chains will generate 2L-αTe. Though the Te-chains remain, the distance between two neighbor chains has shrunk significantly. Interchain distance reduces from 2.7 to 2.43 Å, and the distance between the two nearest interchain atoms also decreases from 3.51 to 3.33 and 3.28 Å (Fig. 1d). In the cross-plane direction (y-axis for bulk Te, z-axis for 2L-αTe), the interlayer distance gets smaller, from 2.34 to 1.81 Å. At the same time, Te-chains also shrink in AC direction (z-axis for bulk Te, y-axis for 2L-αTe), with the lattice parameter decreasing to 5.78 Å in 2L-αTe (Fig. 1f). Angle α of 2L-αTe is 46.976°

Summing up the above, compared to bulk Te, the lattice of 2L-αTe shrinks in all directions. Specifically, in CC direction, lattice constant shrinks from 4.51 Å to 4.33 Å, decreasing by 3.99%, while in AC direction, from 5.96 Å to 5.78 Å, decreasing by 3.02%. The larger lattice shrink makes stronger reinforcement of the bondingin the CC direction. Simultaneously, bond angle α decreases from bulk to 2L-αTe, indicating a stronger interaction in CC direction, too.

Figs. 1(g-j) exhibit the phonon dispersion relations, phonon density of states (PDOS), and the first Brillouin zones (BZs) of bulk Te and 2L-αTe, from which we can see the phonon frequency of bulk Te ranges from 0 to around 4.5 THz while that of 2L-αTe is between 0 and about 4.7 THz. The gap between acoustic branches and optical branches of bulk Te is magnificently larger than that of 2L-αTe. Distinctively, there are several intersections of acoustic and optical branches in the phonon spectrum of 2L-αTe along the

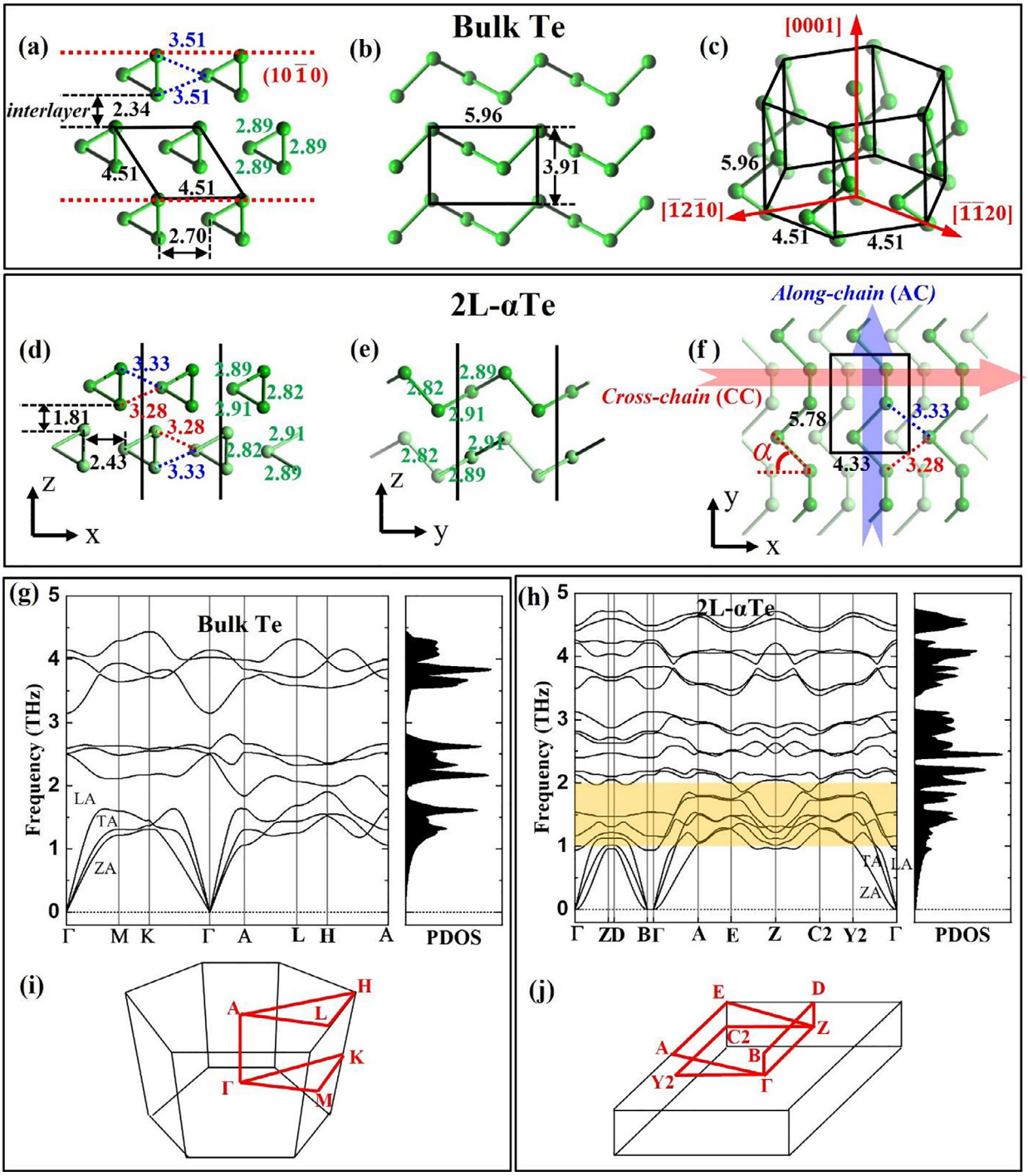

Fig. 1. Lattice structures and phonon spectra of bulk Te and 2L-αTe. (a) (0001) plane, (b) ($\bar{1}2\bar{1}0$) plane, (c) perspective view of bulk Te. (d) (010) plane, (e) (100) plane, (f) (001) plane (in-plane direction) of 2L-αTe. Angle α in (f) is the angle between the Te-Te bond and CC direction. (g) Phonon dispersion relation and PDOS of bulk Te. (h) Phonon dispersion relation and PDOS of 2L-αTe. (i) Brillouin zone of bulk Te. (j) Brillouin zone of 2L-αTe. Black quadrangles in (a, b, f) show the unit cells. Parallel red dot lines in (a) show the cross sections truncating bulk Te to get 2L-αTe. Green numbers denote the length of bonds, blue and red numbers the distances between atoms in angstroms. Double-headed arrow and the black numbers represent the Layer thickness, interchain distance and interlayer distance in angstroms. The red, blue arrow ribbons show the cross-chain (CC, or $\perp$) and along-chain (AC, or $\parallel$) directions, respectively. The highlighted ribbon in (h) shows the range of the low-frequency optical phonons. The red letters and lines in (i) and (j) are the high-symmetry points and paths.

path A-E-Z-C2-Y2, indicating the strong coupling between high-frequency acoustic phonons and low-frequency optical phonons. A similar feature was found in 2D black phosphorus which has a similar layer-stacked structure with 2L-αTe by Hu et al. [29], who name it as "interlayer acoustic-optical phonon-phonon coupling". This feature will create more channels for phonon scattering and will increase the generation of low-frequency optical phonons ranging from 1.0 to 2.0 THz, as highlighted in Fig. 1h . Besides, as a result of the decrease of the interlayer (z-direction) distance, the interlayer CLQB of 2L-αTe is reinforced, thereby the atomic vibrations in the z-direction are strengthened, leading to the stiffening of these low-frequency phonons.

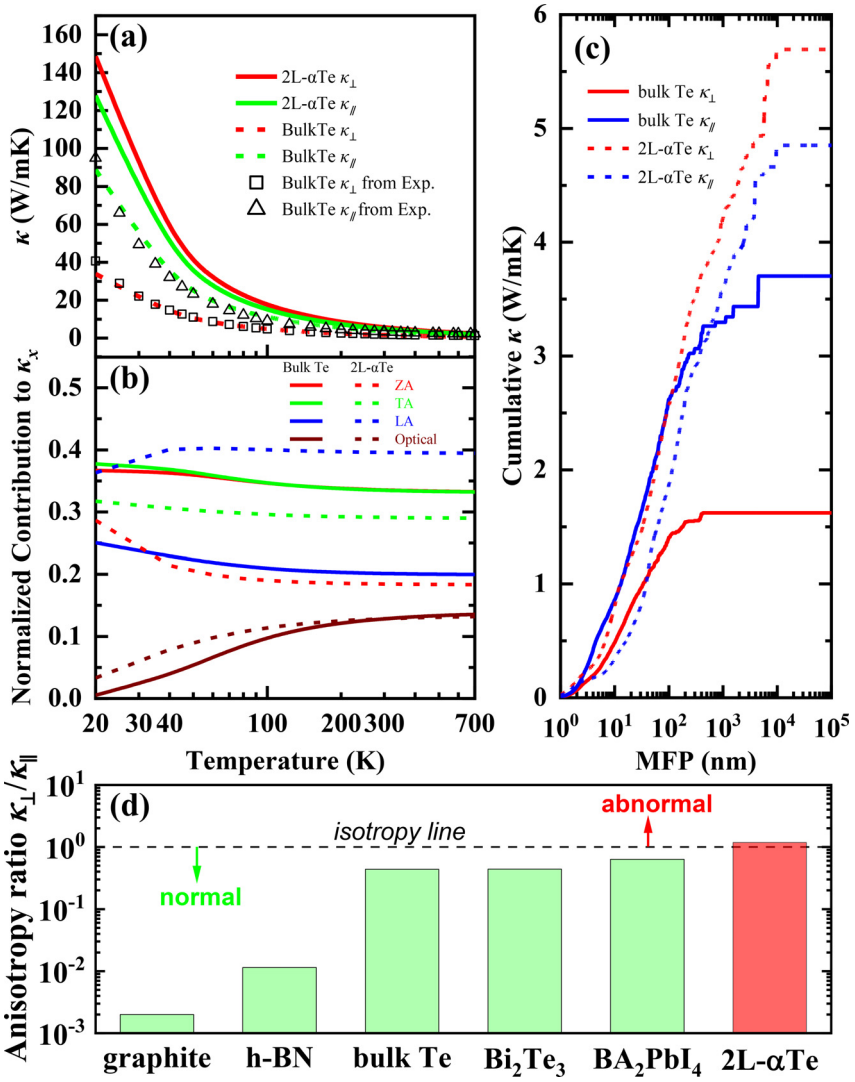

Fig. 2. Lattice Thermal conductivity of bulk Te and 2L-αTe. (a) Our predicted directional lattice thermal conductivity and experimental results [1] versus temperature ranging from 20 to 700 K. (b) Normalized contributions from different phonon branches to thermal conductivity in the x direction at 300 K. (c) Cumulative directional thermal conductivity as a function of phonon mean free path at 300 K. (d) Anisotropy ratio of 2L-αTe compared to different layered materials [25,28,38,41,42].

3.2. Thermal conductivity and the abnormal anisotropy of 2L-αTe

The calculated lattice thermal conductivities of bulk Te and 2L-αTe versus temperature are shown in Fig. 2. As seen in Fig. 2a, the room-temperature lattice thermal conductivities in AC and CC directions of bulk Te are 3.70 W/mK and 1.62 W/mK, respectively, agreeing well with the corresponding values from experiments (3.38 W/mK and 1.97 W/mK) [1]. Thermal conductivities in AC and CC directions of 2L-αTe remain higher than those of bulk Te throughout 20–700 K, with 4.85 W/mK and 5.69 W/mK at room temperature, which are 31% and 251% higher than those of bulk Te, respectively. The enhancement of the thermal conductivity from 3D to the corresponding 2D material also happens in the case from graphite to graphene, where the in-plane room-temperature thermal conductivity rises from 1950 W/mK [38] to around 3000 W/mK [39], with an enhancement of 54%. In graphene, the contribution of ZA mode to the thermal conductivity is the main reason for the in-plane thermal conductivity increase [40]. However, here in 2L-αTe, LA mode, instead of ZA mode, contributes the most to the thermal conductivity at room temperature (Fig. 2b). It is worth noting that all the thermal transport properties calculated in this paper are related to the in-plane direction (Fig. 1f), since the thermal conductivity in out-of-plane direction of 2D materials is physically meaningless. In other words, CC ($\perp$) and AC ($\parallel$) direction are both in-plane.

Fig. 2c shows the cumulative κ as a function of phonon mean free path (MFP) at 300 K, which shows that for 2L-αTe, the $\kappa_\perp$ is slightly higher than $\kappa_\parallel$, opposite to the case in bulk Te. Interestingly and unexpectedly, 2L-αTe shows an abnormal anisotropy ratio $\kappa_\perp/\kappa_\parallel$ of 1.174, as shown in Fig. 2d, distinct from the situation in bulk Te [25] and other layer materials [28,38,41,42]. Especially, before this work, BA_2PbI_4 has been found to has the highest anisotopy ratio (0.633), which is still less than 1, showing a normal anisotropy [28]. The abnormal anisotropy in 2L-αTe challenges our common sense. Intuitively, $\kappa_\perp$ should be prominently lower than $\kappa_\parallel$ due to the weaker vdW interactions in the CC direction than the bonds in the AC direction, just like the situations in all the layered materials with an anisotropy raito lower than 1. This abnormal phenomenon in 2L-αTe will be explored in detail in later sections.

The rest of this paper is organized as follows: in Section 3.3 we would first give an explanation of thermal conductivity enhancement from bulk to 2D systems. Then we would examine the physical origin of abnormal anisotropy in 2L-Te from two perspectives:

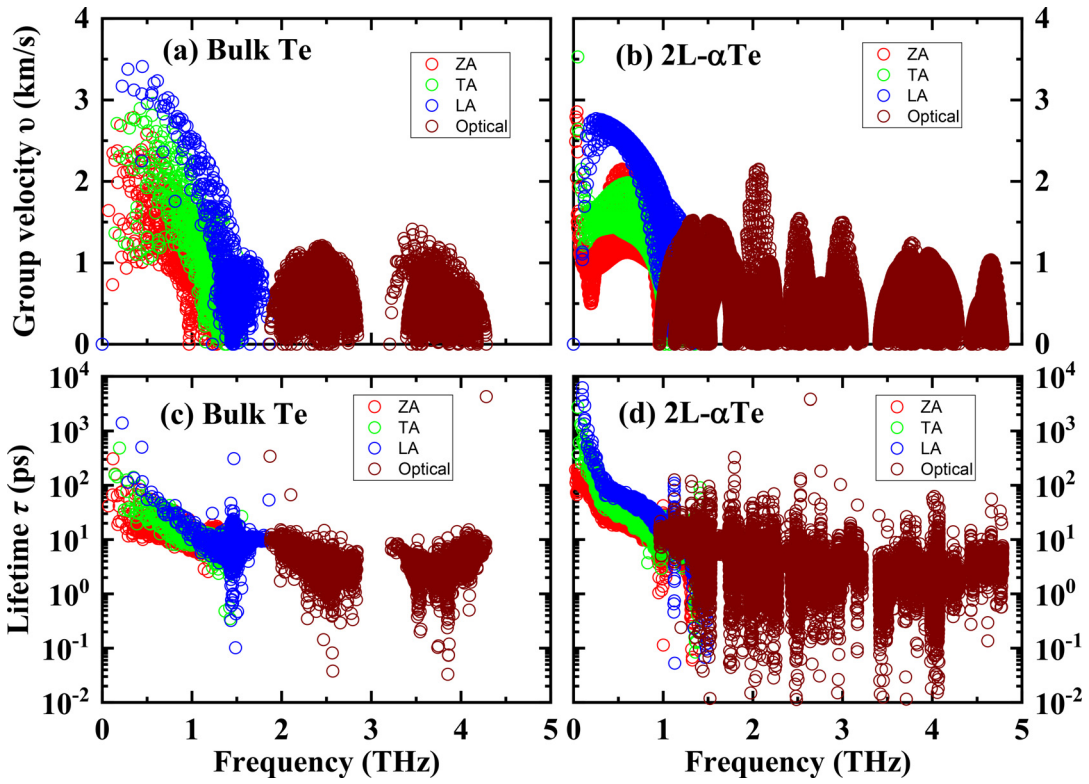

Fig. 3. Frequency-dependent phonon group velocities of bulk Te (a) and 2L-αTe (b); Frequency-dependent phonon lifetimes at room temperature of bulk Te (c) and 2L-αTe (d).

its phonon vibrational properties (Section 3.4) and its bonding nature (Section 3.5).

3.3. Explanation for the enhanced thermal conductivity from bulk to 2L-αTe

According to Eq. (1), higher phonon group velocity υ and longer phonon lifetime τ yield higher thermal conductivity κ. To explain the reason why the $\kappa_{\perp}$ and $\kappa_{\parallel}$ both increase from bulk to 2L-αTe, phonon group velocities and phonon lifetimes of bulk Te and 2L-αTe are illustrated in Fig. 3. We can clearly see that in contrast to bulk Te, 2L-αTe has slightly lower group velocities of acoustic phonons (low-frequency phonons), suggesting that the difference in group velocities is not the cause of the higher thermal conductivity of 2L-αTe. By comparing the lifetimes of acoustic phonons, we find that the average lifetime of acoustic phonons in 2L-αTe is around 50 ps, considerably larger than that of bulk Te with $\sim$ 10 ps, indicating that the longer lifetime is key to the higher thermal conductivity of 2L-αTe.

To further explore the source of the longer phonon lifetime of 2L-αTe, the Grüneisen parameters and phase space are displayed in Fig. 4. It can be seen that the amplitudes of the overall Grüneisen parameters of bulk Te are higher than those of 2L-αTe, confirming stronger phonon anharmonicity in bulk Te. However, the phase space of 2L-αTe is slightly higher than that of bulk Te, indicating more three-phonon scattering channels in 2L-αTe than in bulk Te. Considering the collective impact of Grüneisen parameters and phase space, the longer phonon lifetimes of 2L-αTe are attributed to the weaker anharmonicity instead of the larger number of three-phonon scattering channels as compared to the bulk Te. According to the potential energy well analysis in the Fig. S2, from bulk Te to 2L-αTe, the phonon anharmonicity gets weaker in CC direction, and stronger in AC direction, which implies that the anharmonicity in CC direction dominates the impact on thermal conductivity. As aforementioned, the lattice shrink is larger in the CC direction, and the angle α is smaller in 2L-αTe, which reinforce the CLQB in CC direction, leading to the weaker anharmonicity of 2L-αTe.

3.4. Vibrational origin of the abnormal anisotropy of 2L-αTe

To explore the vibrational origin of the anomalous in-plane thermal conductivity anisotropy of 2L-αTe, the fitted average directional phonon group velocity and directional cumulative κ versus phonon frequency are plotted in Fig. 5a. Detail of the derivation of the average direction group velocity is illustrated in Supporting Information. It can be seen that $\upsilon_{\parallel}$ is initially higher than $\upsilon_{\perp}$ but then becomes lower when the frequency exceeds 1.0 THz. According to Eq. (1), higher phonon group velocity υ yields higher thermal conductivity κ. Hence, within the frequency range from 1.0 to 2.0 THz, cumulative thermal conductivity in CC direction, $\kappa_{\perp}$, shows a steeper slope than that in AC direction, $\kappa_{\parallel}$. Interestingly, this frequency range from 1.0 to 2.0 THz is exactly where high-frequency LA modes and low-frequency optical modes locate, as highlighted in Fig. 1(h). This indicates that the higher $\kappa_{\perp}$ is attributed to higher group velocity of the high-frequency acoustic and low-frequency optical phonons.

Directional phonon lifetime is another property that impacts the anisotropy. The definition of the directional phonon lifetime is demonstrated in Supporting Information. According to Eq. (1), longer phonon lifetime τ yields higher thermal conductivity κ. Figs. 5b exhibits the frequency-dependent directional phonon lifetimes in 0–3.0 THz of 2L-αTe, where a prominent gap between $\tau_{\perp}$ and $\tau_{\parallel}$ emerges in the frequency range of 1.5–1.8 THz while $\tau_{\parallel}$ is almost zero. Intriguingly, as aforementioned, the group velocity gap happens in this frequency range as well (Fig. 5a). The lifetimes of 2L-αTe maintain overall equal in two directions in the frequency range other than 1.5–1.8 THz. Therefore, longer $\tau_{\perp}$ in the frequency range of 1.5–1.8 THz is another reason for the abnormal thermal anisotropy of 2L-αTe.

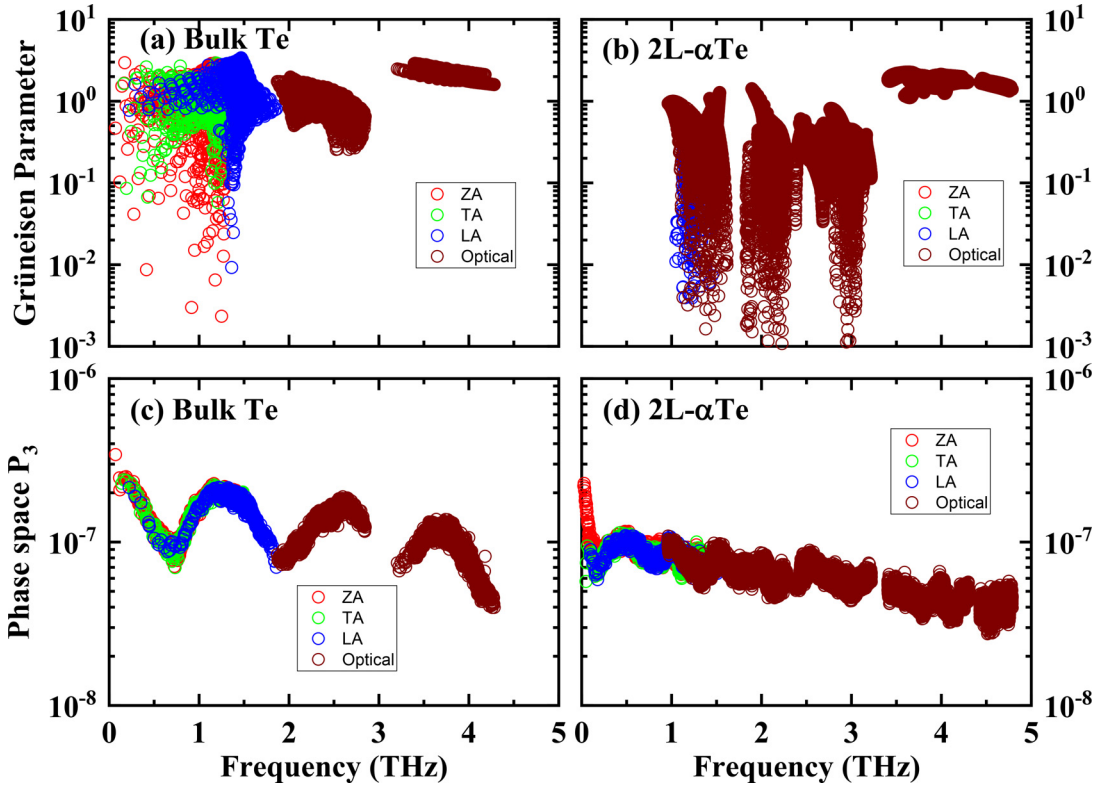

Fig. 4. Frequency-dependent Grüneisen parameter of bulk Te (a) and 2L-αTe (b); Frequency-dependent Phase space of bulk Te (c) and 2L-αTe (d).

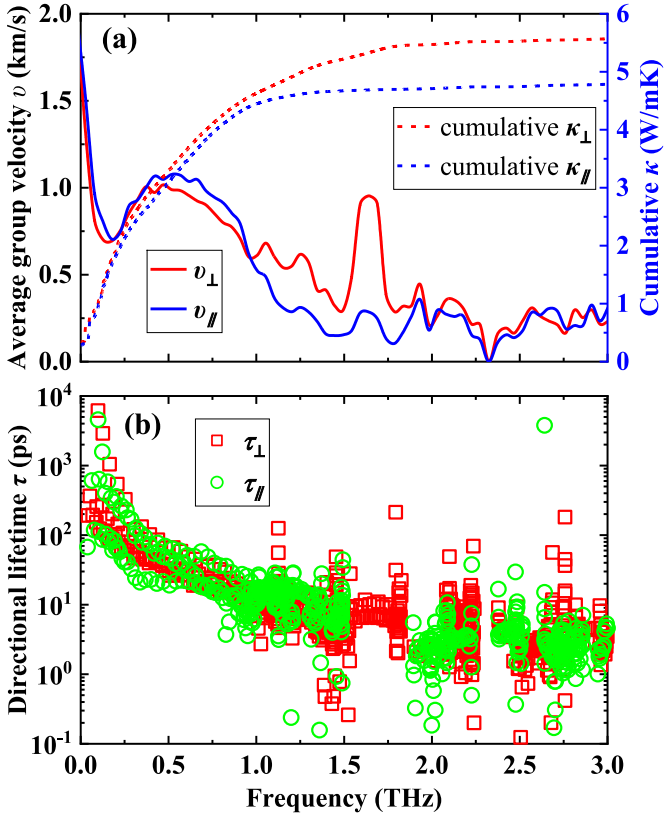

Fig. 5. (a) Fitted directional average phonon group velocity and cumulative κ of 2L-αTe. (b) Directional phonon lifetime of 2L-αTe.

In short, the abnormal anisotropy of 2L-αTe is attributed to the higher phonon group velocity and longer phonon lifetime in the CC direction. Based upon the lattice structure and phonon dispersion analysis in Section 3.1, we can now connect lattice change with the abnormal anisotropy. As mentioned before, the larger shrink in CC direction and the decrease of the angle α lead to enhancement of the strength of CLQB of 2L-αTe in CC direction, which in turn stiffen the phonons and weaken the phonon anharmonicity in CC direction. Subsequently, the phonon group velocity rises and the phonon lifetime increases in CC direction, resulting in the higher thermal conductivity in CC direction than in AC direction, i.e., the abnormal anisotropy of 2L-αTe.

3.5. Electronic origin of the abnormal thermal anisotropy of 2L-αTe

To further explore the electronic origin of the enhancement of CLQB in CC direction, the orbital projected electronic band structures and projected density of states (pDOS) [43] are analyzed, as shown in Fig. 6(a, b, f, g). The band gap broadens from 0.1176 eV in bulk Te to 1.021 eV in 2L-αTe, which shows more non-metal-like feature, resulting in an enhancement of atomic insteraction. The pDOS of the three 5p orbitals become more uniform and mixed from bulk to 2L-αTe below the Fermi level, impling that a stronger sp^3 hybridization intensifies the CLQB.

To intuitively show the strength of the Te-Te interactions in AC and CC direction, the projected crystal orbital Hamilton population (COHP), integrated projected COHP (IpCOHP) and electron localization function (ELF) are shown in Fig. 6(c-e, h-j). The COHP is a quantitative method to measure the bonding strength between atom pairs, through analyzing the bonding and antibonding states below Fermi level [44]. A negative COHP corresponds to bonding state and lowers the system energy whereas a positive COHP corresponds to antibonding state and increases the system energy. Te-Te bonding state COHP and IpCOHP are higher in AC direction than

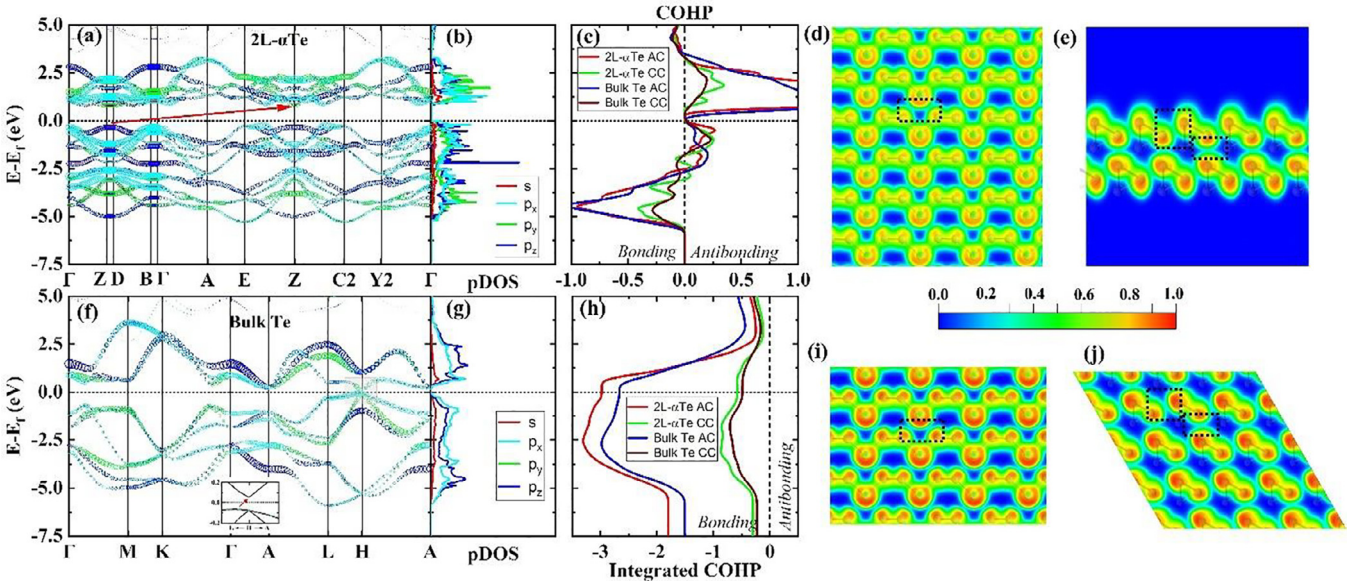

Fig. 6. Orbital projected electronic band structure and pDOS, projected COHP (c) and integrated projected COHP (h) for Te-Te interaction in AC and CC direction, and ELF distributions for 2L-αTe (a-e, h) and bulk Te (c, f-j). Red arrows in (a) and (f) show the band gaps. The inset in (f) is the zoom-in of the band gap area. (d) (001) plane and (e) (010) plane of ELF for 2L-αTe. (i) $(10\bar{1}0)$ plane and (j) (0001) plane of ELF for bulk Te. Black squares in (d, e, i, j) surround the transition area between interchains.
Note: pDOS curves of the p_x and the p_y orbitals for bulk Te (g) are totally overlapped, as a result, the p_y orbital cannot be observed in the figure.

CC, proving that Te-Te connection is bond in AC direction and CLQB in CC direction, as shown in Fig. 6c, h. Te-Te COHP and IpCOHP in CC direction are significantly higher for 2L-αTe than for bulk, which indicates the enhancement of the CLQB in CC direction. To show the percentage of strength increase of the Te-Te interaction in CC and AC direction, we compare the IpCOHP values at the Fermi level reference line in Fig. 6h. The values of bulk CC and 2L-αTe CC are -0.494 and -0.602, respectively, increasing by 21.9%; while the values of bulk AC and 2L-αTe AC are -2.667 and -2.985, respectively, increasing by 11.9%. Apparently, the reinforce of the interaction is significantly larger in CC direction than in AC direction, which is consistent with the situation in lattice shrink.

ELF distribution is another way to reflect the strength of interaction. ELF varies from 0 to 1, where 0 means no electron localized and 1 corresponds to perfect localization. The greater the ELF value is, the higher the electron localization degree is, and the stronger the interactions (CLQB in CC direction for this case) are. It can be seen that ELF in CC direction of 2L-αTe (Fig. 6d, e) is higher than that of bulk (Fig. 6i, j), demonstrating the stronger CLQB of 2L-αTe than of bulk.As aforementioned, the strong interchain interaction is the CLQB, which was firstly found in 2D black phosphorus [29] and few-layer tellurene [11] and attributed to wavefunction hybridization. We believe the electron pDOS blow the Fermi level (Fig. 6b, g) and the interchain transition area in ELF of 2L-αTe (Fig. 6d, e) is the evidence of wavefunction hybridization. Simutaneouly, with the wavefunction hybridization, lone electron pair forms in Te-Te atom pairs. The valence electrons of Te are $5s^2 5p^4$, six electrons in total, four of which occupy two sp^3 hybrid orbitals and form σ bonds with adjacent atoms in the chain, the other two form the lone electron pair in another sp^3 orbital. In the CC and interlayer direction, lone electron pairs of the nearest neighbors interact with each other, providing additional interation, which also enhance the CLQB.

We collect the reported thermal conduvtivities of α-phase Te from bilayer to bulk in Fig. S3. Although the intrinsic thermal conductivities of 3-layer, 4-layer, or multi-layer tellurene are not accessible by first-principles calculation within our current computation capability, we can gain some clue about the thickness-dependent property of the thermal conductivity anisotropy by the comparison between 2L-αTe, multilayer α-Te, and bulk Te: starting from 2L-αTe, with the increase of the number of layers, $\kappa_\perp$ would be initially greater than $\kappa_\parallel$, then become smaller than it, and finally recover the normal thermal anisotropy in bulk Te. This dimensional crossover behavior has been also found in Bi_2Te_3 films [45], which results from the interplay between phonon Umplapp scattering and boundary scattering. Based on the Fig. S3, we believe that the transition of α-phase Te from abnormal to normal thermal anisotropy happens between 3 to $\sim$30 layers, i.e., the unexplored region in Fig. S3.

4. Conclusion

In summary, we study the thermal transport properties of the thinnest stable α-phase tellurene, 2L-αTe, by employing first-principles calculations. For comparison, the thermal transport properties of bulk Te are also investigated. The thermal conductivities of 2L-αTe are higher than those of bulk Te in both AC and CC direction by 31% and 251%, respectively. The enhanced thermal conductivity is originated from the longer phonon lifetime of 2L-αTe, which are attributed to the weaker anharmonicity in CC direction. Unexpectedly, $\kappa_\perp$ is larger than $\kappa_\parallel$ for 2L-αTe, leading to an anomalous thermal conductivity anisotropy. To gain insight into the microscopic mechanisms behind the enhanced thermal conductivity and the anomalous anisotropy from bulk Te to 2L-αTe, we further analyze the lattice structure, phonon spectrum, and phonon properties. The direct reason for the abnormal anisotropy are the higher phonon group velocity and longer phonon lifetime in CC direction of 2L-αTe, which are attributed to the stiffened phonon and weaker phonon anharmonicity, especially for the high-frequency LA modes and low-frequency optical modes ranging from 1.0 to 2.0 THz. The weaker anharmonicity and the stiffness of phonon are caused by the larger lattice shrink in CC direction and the bond angle change. Electron band structure, pDOS, COHP, IpCOHP, and ELF of 2L-αTe and bulk Te are further analyzed to obtain deeper understanding. The enhancement of CLQB are demonstrated. The origin of CLQB is discussed, which results from the wavefunction hybridization and lone electron pair interaction. Our study provides the comprehensive understanding for thermal

transport properties of 2L-αTe, uncovers the origin of anomalous thermal conductivity anisotropy in 2D Te, and sheds light to the thermal management for electronic devices of other 2D materials.

Declaration of Competing Interest

The authors declare that they have no known competing financial interests or personal relationships that could have appeared to influence the work reported in this paper.

CRediT authorship contribution statement

Yanhua Cheng: Data curation, Investigation, Visualization, Writing – original draft. **Xiaolong Yang:** Formal analysis, Methodology, Writing – review & editing. **Zherui Han:** Methodology. **Wenzhuo Wu:** Funding acquisition, Validation. **Xiaobing Luo:** Funding acquisition, Supervision. **Xiulin Ruan:** Conceptualization, Supervision, Writing – review & editing.

Acknowledgement

Y. C. acknowledges the support from the China Scholarship Council (No. 201906160050). X. L. acknowledges the support from the National Natural Science Foundation of China (No. 51625601 and 52076087). Simulations have been performed at the Rosen Center of Advanced Computing at Purdue University. W. W. acknowledges the support by NSF under grant No. CMMI-1762698.

Supplementary materials

Supplementary material associated with this article can be found, in the online version, at doi:10.1016/j.ijheatmasstransfer.2022.122908.

References

[1] C.Y. Ho, R.W. Powell, P.E. Liley, Thermal conductivity of the elements, J. Phys. Chem. Ref. Data 1 (2) (1972) 279–421.
[2] Z. Zhu, X. Cai, S. Yi, J. Chen, Y. Dai, C. Niu, Z. Guo, M. Xie, F. Liu, J.H. Cho, Y. Jia, Z. Zhang, Multivalency-driven formation of te-based monolayer materials: a combined first-principles and experimental study, Phys. Rev. Lett. 119 (10) (2017) 106101.
[3] Y. Dong, B. Zeng, X. Zhang, D. Li, J. He, M. Long, Study on the strain-induced mechanical property modulations in monolayer Tellurene, J Appl Phys 125 (6) (2019).
[4] K.V. Sopiha, O.I. Malyi, C. Persson, First-principles mapping of the electronic properties of two-dimensional materials for strain-tunable nanoelectronics, ACS Appl. Nano Mater. 2 (9) (2019) 5614–5624.
[5] Y. Wang, S. Yao, P. Liao, S. Jin, Q. Wang, M.J. Kim, G.J. Cheng, W. Wu, Strain-engineered anisotropic optical and electrical properties in 2D chiral-chain tellurium, Adv. Mater. 32 (29) (2020) e2002342.
[6] Y. Xiang, S. Gao, R.-.G. Xu, W. Wu, Y. Leng, Phase transition in two-dimensional tellurene under mechanical strain modulation, Nano Energy 58 (2019) 202–210.
[7] X.X. Xue, Y.X. Feng, L. Liao, Q.J. Chen, D. Wang, L.M. Tang, K. Chen, Strain tuning of electronic properties of various dimension elemental tellurium with broken screw symmetry, J. Phys. Condens. Matter 30 (12) (2018) 125001.
[8] J. Ma, F. Meng, J. He, Y. Jia, W. Li, Strain-induced ultrahigh electron mobility and thermoelectric figure of merit in monolayer α-Te, ACS Appl. Mater. Interfaces 12 (39) (2020) 43901–43910.
[9] X. Cai, Y. Ren, M. Wu, D. Xu, X. Luo, Strain-induced phase transition and giant piezoelectricity in monolayer tellurene, Nanoscale 12 (1) (2020) 167–172.
[10] Y. Wang, C. Xiao, M. Chen, C. Hua, J. Zou, C. Wu, J. Jiang, S.A. Yang, Y. Lu, W. Ji, Two-dimensional ferroelectricity and switchable spin-textures in ultra-thin elemental Te multilayers, Mater. Horiz. 5 (3) (2018) 521–528.
[11] J. Qiao, Y. Pan, F. Yang, C. Wang, Y. Chai, W. Ji, Few-layer Tellurium: one-dimensional-like layered elementary semiconductor with striking physical properties, Sci. Bull. 63 (3) (2018) 159–168.
[12] B. Wu, X. Liu, J. Yin, H. Lee, Bulkβ-Te to few layeredβ-tellurenes: indirect to direct band-Gap transitions showing semiconducting property, Mater. Res. Express 4 (9) (2017).
[13] L. Tong, X. Huang, P. Wang, L. Ye, M. Peng, L. An, Q. Sun, Y. Zhang, G. Yang, Z. Li, F. Zhong, F. Wang, Y. Wang, M. Motlag, W. Wu, G.J. Cheng, W. Hu, Stable mid-infrared polarization imaging based on quasi-2D tellurium at room temperature, Nat. Commun. 11 (1) (2020) 2308.
[14] J.-.K. Qin, P.-.Y. Liao, M. Si, S. Gao, G. Qiu, J. Jian, Q. Wang, S.-.Q. Zhang, S. Huang, A. Charnas, Y. Wang, M.J. Kim, W. Wu, X. Xu, H.-.Y. Wang, L. Yang, Y. Khin Yap, P.D. Ye, Raman response and transport properties of tellurium atomic chains encapsulated in nanotubes, Nat. Electron. (2020).
[15] C. Lin, W. Cheng, G. Chai, H. Zhang, Thermoelectric properties of two-dimensional selenene and tellurene from group-VI elements, Phys. Chem. Chem. Phys. 20 (37) (2018) 24250–24256.
[16] Z. Gao, G. Liu, J. Ren, High thermoelectric performance in two-dimensional tellurium: an Ab initio study, ACS Appl. Mater. Interfaces 10 (47) (2018) 40702–40709.
[17] D.K. Sang, T. Ding, M.N. Wu, Y. Li, J. Li, F. Liu, Z. Guo, H. Zhang, H. Xie, Monolayer beta-tellurene: a promising p-type thermoelectric material via first-principles calculations, Nanoscale 11 (39) (2019) 18116–18123.
[18] G. Qiu, S. Huang, M. Segovia, P.K. Venuthurumilli, Y. Wang, W. Wu, X. Xu, P.D. Ye, Thermoelectric performance of 2D tellurium with accumulation contacts, Nano Lett. 19 (3) (2019) 1955–1962.
[19] S. Lin, W. Li, Z. Chen, J. Shen, B. Ge, Y. Pei, Tellurium as a high-performance elemental thermoelectric, Nat. Commun. 7 (2016) 10287.
[20] Y. Wang, G. Qiu, R. Wang, S. Huang, Q. Wang, Y. Liu, Y. Du, W.A. Goddard, M.J. Kim, X. Xu, P.D. Ye, W. Wu, Field-effect transistors made from solution-grown two-dimensional tellurene, Nat. Electron. 1 (4) (2018) 228–236.
[21] C. Yan, C. Wang, L. Zhou, P. Guo, K. Liu, Z.-.Y. Lu, Z. Cheng, Y. Chai, A. Pan, W. Ji, Two ultra-stable novel allotropes of tellurium few-layers, Chin. Phys. B 29 (9) (2020).
[22] G. Liu, Z. Gao, J. Ren, Anisotropic thermal expansion and thermodynamic properties of monolayer β-Te, Phys. Rev. B 99 (19) (2019).
[23] S. Sharma, N. Singh, U. Schwingenschlögl, Two-dimensional tellurene as excellent thermoelectric material, ACS Appl. Energy Mater. 1 (5) (2018) 1950–1954.
[24] Z. Gao, F. Tao, J. Ren, Unusually low thermal conductivity of atomically thin 2D tellurium, Nanoscale 10 (27) (2018) 12997–13003.
[25] S. Huang, M. Segovia, X. Yang, Y.R. Koh, Y. Wang, P.D. Ye, W. Wu, A. Shakouri, X. Ruan, X. Xu, Anisotropic thermal conductivity in 2D tellurium, 2D Mater. 7 (1) (2019).
[26] Y.S. Xie, T.Y. Wang, B.W. Zhu, C.Y. Yan, P.X. Zhang, X.W. Wang, G. Eres, 19-Fold thermal conductivity increase of carbon nanotube bundles toward high-end thermal design applications, Carbon N Y 139 (2018) 445–458.
[27] A. Alofi, G.P. Srivastava, Thermal conductivity of graphene and graphite, Phys. Rev. B 87 (11) (2013).
[28] C. Li, H. Ma, T. Li, J. Dai, M.A.J. Rasel, A. Mattoni, A. Alatas, M.G. Thomas, Z.W. Rouse, A. Shragai, S.P. Baker, B.J. Ramshaw, J.P. Feser, D.B. Mitzi, Z. Tian, Remarkably weak anisotropy in thermal conductivity of two-dimensional hybrid perovskite Butylammonium lead iodide crystals, Nano Lett. 21 (9) (2021) 3708–3714.
[29] Z.X. Hu, X. Kong, J. Qiao, B. Normand, W. Ji, Interlayer electronic hybridization leads to exceptional thickness-dependent vibrational properties in few-layer black phosphorus, Nanoscale 8 (5) (2016) 2740–2750.
[30] J.M. Ziman, Electrons and Phonons: The Theory of Transport Phenomena in Solids, Clarendon Press, 1960.
[31] D.A. Broido, L. Lindsay, A. Ward, Thermal conductivity of diamond under extreme pressure: a first-principles study, Phys. Rev. B 86 (11) (2012) 115203.
[32] G. Kresse, J. Furthmuller, Efficient iterative schemes for ab initio total-energy calculations using a plane-wave basis set, Phys. Rev. B Condens. Matter. 54 (16) (1996) 11169–11186.
[33] G. Kresse, D. Joubert, From ultrasoft pseudopotentials to the projector augmented-wave method, Phys. Rev. B 59 (3) (1999) 1758–1775.
[34] J.P. Perdew, K. Burke, M. Ernzerhof, Generalized gradient approximation made simple (vol 77, pg 3865, 1996), Phys. Rev. Lett. 78 (7) (1997) 1396-1396.
[35] Chevary Perdew, Jackson Vosko, Singh Pederson, Fiolhais, Atoms, molecules, solids, and surfaces: applications of the generalized gradient approximation for exchange and correlation, Phys. Rev., B Condens. Matter 46 (11) (1992) 6671–6687.
[36] A. Togo, I. Tanaka, First principles phonon calculations in materials science, Scr. Mater. 108 (2015) 1–5.
[37] W. Li, J. Carrete, N.A. Katcho, N. Mingo, ShengBTE: a solver of the Boltzmann transport equation for phonons, Comput. Phys. Commun. 185 (6) (2014) 1747–1758.
[38] G.A. Slack, Anisotropic thermal conductivity of pyrolytic GRAPHITE, Phys. Rev. 127 (3) (1962) 694–701.
[39] A. Alofi, G.P. Srivastava, Phonon conductivity in graphene, J. Appl. Phys. 112 (1) (2012) 013517.
[40] L. Lindsay, D.A. Broido, N. Mingo, Flexural phonons and thermal transport in graphene, Phys. Rev. B 82 (11) (2010).
[41] H.J. Goldsmid, The thermal conductivity of bismuth telluride, Proc. Phys. Soc. London Sect. B 69 (2) (1956) 203–209.
[42] P. Jiang, X. Qian, R. Yang, L. Lindsay, Anisotropic thermal transport in bulk hexagonal boron nitride, Phys. Rev. Mater. 2 (6) (2018).
[43] V. Wang, N. Xu, J.-.C. Liu, G. Tang, W.-.T. Geng, VASPKIT: a user-friendly interface facilitating high-throughput computing and analysis using VASP code, Comput. Phys. Commun. 267 (2021).
[44] S. Maintz, V.L. Deringer, A.L. Tchougreeff, R. Dronskowski, LOBSTER: a tool to extract chemical bonding from plane-wave based DFT, J. Comput. Chem. 37 (11) (2016) 1030–1035.
[45] B. Qiu, X. Ruan, Thermal conductivity prediction and analysis of few-quintuple Bi2Te3 thin films: a molecular dynamics study, Appl. Phys. Lett. 97 (18) (2010).